KSME

Springer

Journal of Mechanical Science and Technology 34 (1) 2020

Original Article
DOI 10.1007/s12206-019-1233-x

Keywords:
· 3D ultrasonic vibration
· ELID grinding
· Grinding force
· Kinematics analysis
· Surface quality
· Ultrasonic vibration-assisted grinding

Correspondence to:
Guangxi Li
pdsukyc08@126.com

Citation:
Chen, F., Mei, G., Zhao, B., Bie, W., Li, G. (2020). Study on the characteristics of zirconia ceramic in three-dimensional ultrasonic vibration-assisted ELID internal grinding. Journal of Mechanical Science and Technology 34 (1) (2020) 333-344. http://doi.org/10.1007/s12206-019-1233-x

Received May 17th, 2019
Revised August 12th, 2019
Accepted October 15th, 2019

† Recommended by Editor Yang Na

Study on the characteristics of zirconia ceramic in three-dimensional ultrasonic vibration-assisted ELID internal grinding

Fan Chen[1], Guojian Mei[2], Bo Zhao[3], Wenbo Bie[1,3] and Guangxi Li[1]

[1]School of Electrical and Mechanical Engineering, Pingdingshan University, Pingdingshan, 467000, China, [2]Henan Zhongyuan Ancient Ceramic Key Laboratory, Pingdingshan University, Pingdingshan, 467000, China, [3]School of Mechanics and Power Engineering, Henan Polytechnic University, Jiaozuo, 454003, China

Abstract Three-dimensional (3D) ultrasonic vibration-assisted ELID grinding, which combines 3D ultrasonic vibration-assistance with electrolytic in-process grinding wheel dressing (ELID), is a compound process that is designed to achieve high-efficiency precision machining. A grinding force model of 3D ultrasonic vibration-assisted ELID grinding was first developed on the basis of the kinematics of a single grit particle and was verified through experimentation. The surface quality then was observed using white light interference profiling. It was demonstrated during the present investigation that the grinding force during 3D ultrasonic vibration-assisted ELID grinding was approximately 20 %~30 % lower than that of two-dimensional (2D) ultrasonic vibration-assisted ELID grinding. In addition, the surface roughness (Ra) achieved during 3D ultrasonic vibration-assisted ELID grinding was approximately 40 %~50 % smoother than was achieved under 2D ultrasonic vibration-assisted ELID, and thus 3D ultrasonic vibration-assisted ELID grinding can achieve better surface quality.

1. Introduction

Zirconia ceramics, as hard-brittle materials, are widely used for their particular properties, such as high strength, hardness, wear- and corrosion-resistance. However, it is difficult for conventional machining to process due to their high brittleness, low fracture toughness and an elastic limit that is close to their maximum tensile strength [1-3]. In recent years, ultrasonic vibration-assisted grinding has emerged as a more sophisticated method for the processing of zirconia ceramics. It can increase the critical grinding depth, achieve greater ductile regime machining, extend the life of the grinding wheel, reduce surface roughness and enhance surface quality [4, 5]. It is known that the 2D ultrasonic vibration-assisted ELID grinding can expand the scope of ceramic plastic region grinding and improve the quality of the processed surface [6, 7]. Whether 3D ultrasonic vibration-assisted ELID grinding is feasible and will make best use of both the advantages of ultrasonic vibration and of grinding wheel electrolytic in-process dressing (ELID) has not been concluded. In consequence, the present study should be of value for clarifying machining theory of 3D ultrasonic vibration-assisted ELID grinding and researching practical application of the technology for precision grinding of hard-brittle materials.

Grinding force is one of the most fundamental characteristics that affect the process and influences mainly the manufacturing accuracy and surface quality [8]. It is of great benefit, therefore, to study the effects of grinding force during ultrasonic vibration-assisted grinding of ceramic materials. In the present study, the grinding force during 3D ultrasonic vibration-assisted ELID grinding was first established on the basis of the kinematics of a single grit particle. The surface quality was observed using white light interference surface profilometry. The outcome of the investigation should be useful during future research into ultrasonic vibration-assisted ELID grinding.

The report is presented in six sections. Following this introduction section, Sec. 2 describes

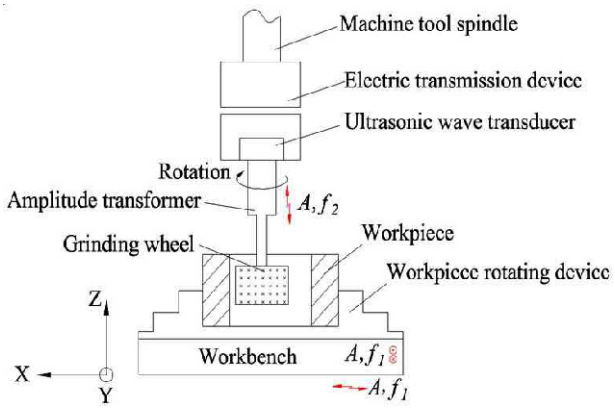

Fig. 1. Schematic diagram of 3D ultrasonic vibration-assisted internal grinding.

the equivalent structure of 3D ultrasonic vibration-assisted ELID internal grinding. The analysis of grinding force in 3D ultrasonic vibration-assisted ELID internal grinding is given in Sec. 3. In Sec. 4, experimental tests and analyses of grinding force are reported, and surface quality analysis after 3D ultrasonic vibration-assisted internal grinding is presented. Conclusions from the investigation are given in Sec. 5.

2. Equivalent structure of 3D ultrasonic vibration-assisted ELID internal grinding

A schematic diagram to illustrate 3D ultrasonic vibration-assisted internal grinding is given in Fig. 1. As shown, the grinding wheel processes the internal surface (bore) of the workpiece along the Z direction, and the workpiece is rotated by the workpiece rotating device mounted on the workbench. In 3D ultrasonic vibration-assisted ELID internal grinding, the workpiece is driven in simple harmonic oscillation along X and Y direction. At the same time, the grinding wheel is subjected to Z-directional ultrasonic vibration. When the workpiece is vibrated along two axes, the ultrasonic generator should provide two identical frequency excitation signals for realization the 2D elliptical vibrations. Initially, although wireless transmission was employed to supply the power to the ultrasonic vibration system, the precision speed-regulation motor was not sufficiently powerful to cope with the overall weight of the device, workpiece, and the 2D ultrasonic vibration system. It was difficult, therefore, for the machine to run stably or to move normally, and therefore a 3D ultrasonic vibration-assisted ELID internal grinding was proposed for the present study to allow the mechanism of 3D ultrasonic vibration-assisted ELID grinding to be investigated.

The processed surface of the ceramic specimen is equivalent to an extension of the local contact between the grinding wheel and the bore of the workpiece in 3D ultrasonic vibration-assisted internal grinding, as shown in Fig. 2. The advantages of equivalent structure are as follows [9]:

(1) Rotation of workpiece is simplified into a straight reciprocating motion of the workbench.

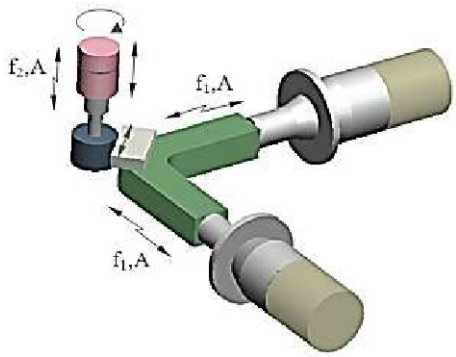

Fig. 2. Equivalent schematic diagram for 3D ultrasonic vibration-assisted internal grinding.

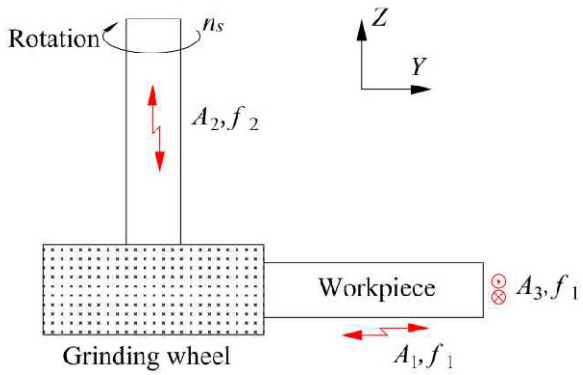

Fig. 3. Schematic diagram of 3D ultrasonic vibration-assisted ELID internal grinding.

(2) It allows the surface appearance and roughness to be observed after the workpiece is processed.

(3) It is convenient also to monitor the grinding force, temperature, and ultrasonic cavitation behavior during the grinding procedure.

3. Analysis of the grinding force during 3D ultrasonic vibration-assisted ELID internal grinding

3.1 The kinematics analysis of single diamond grit particle trajectory

As the grinding wheel rotates and feeds along the Z direction, as shown in Fig. 3, the side of the workpiece is processed by the grinding wheel and the workpiece is fed along the X direction of the workbench, which is subjected to, and is parallel to, the 2D ultrasonic vibration in the X and Y directions during the 3D ultrasonic vibration-assisted internal grinding. The trajectory of a single diamond grit particle is a compound of the rotation, feed movement and ultrasonic vibration of the grinding wheel. This assumption is justified as follows [10]:

(1) The amplitude and frequency of ultrasonic vibration remain fairly stable.

(2) The reciprocating linear velocity of the workbench re-

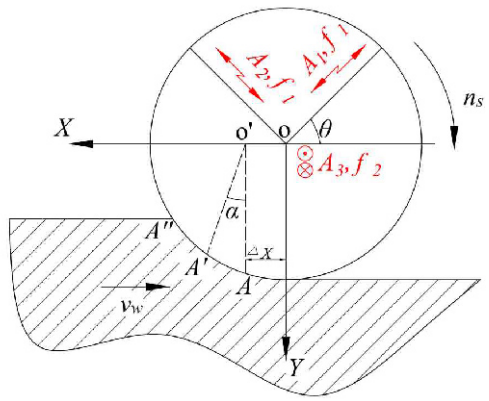

Fig. 4. Cutting model for a single diamond grit particle.

mains unchanged.

(3) The diamond grit is distributed evenly on the circumference of grinding wheel.

(4) The characteristics of the workpiece material are continuous, homogeneous and isotropic.

(5) The ceramic materials is removed by plastic removal during the grinding process.

In the sketch of 3D ultrasonic vibration-assisted ELID internal grinding, the cutting model of a single diamond grit particle is proposed as shown in Fig. 4. If the grinding wheel is regarded as a particle when the specific simple harmonic is superimposed, the particle trajectory can be expressed as:

$$\begin{cases} x' = A_1\cos(2\pi f_1 t+\varphi_1)\cos\theta + A_2\cos(2\pi f_1 t+\varphi_2)\sin\theta \\ y' = A_1\cos(2\pi f_1 t+\varphi_1)\sin\theta + A_2\cos(2\pi f_1 t+\varphi_2)\cos\theta \\ z' = A_3\cos(2\pi f_2 t+\varphi_3) \end{cases} \quad (1)$$

where x', y' and z' denote the particle trajectory in the *X*, *Y*, Z directions, respectively; f_1 is the frequency of 2D ultrasonic vibration on the workbench with synchronous vibration; f_2 is the frequency in the *Z* direction, *θ* is the fixed angle of L-shaped plate with a two-dimensional ultrasound device on it; A_1, A_2 and A_3 denote the ultrasonic amplitude in the *X*, *Y*, *Z* directions, respectively; and φ_1, φ_2 and φ_3 are the 3D ultrasonic vibration phase angles, respectively.

It is assumed that the single diamond grit particle begins to contact with the workpiece at point A at t_0, then reaches point A' at *t*, and detaches from workpiece at point A". Taking the time from contact to separation into consideration, the grit movement could be broken down into a horizontal displacement of Δx and then turned *α* around the O´, including:

$$\begin{cases} \Delta x = V_w(t-t_0) \\ \alpha = \omega(t-t_0) \\ \omega = 2V_s/d_s \end{cases} \quad (2)$$

where V_W is the speed of the workpiece; V_S is the speed of grinding wheel; ω is the angular speed of the grinding wheel, and ds is the diameter of the grinding wheel.

According to Eq. (1), the $\Delta Ax'$, $\Delta Ay'$ and $\Delta Az'$ increase due to the ultrasonic vibration, from contact to separation, can be expressed as:

$$\begin{cases} \Delta Ax' = A_1\cos\theta\left[\cos(2\pi f_1 t+\varphi_1)-\cos(2\pi f_1 t_0+\varphi_1)\right]+ \\ \qquad A_2\sin\theta\left[\cos(2\pi f_1 t+\varphi_2)-\cos(2\pi f_1 t_0+\varphi_2)\right] \\ \Delta Ay' = A_1\sin\theta\left[\cos(2\pi f_1 t+\varphi_1)-\cos(2\pi f_1 t_0+\varphi_1)\right]+ \\ \qquad A_2\cos\theta\left[\cos(2\pi f_1 t+\varphi_2)-\cos(2\pi f_1 t_0+\varphi_2)\right] \\ \Delta Az' = A_3\left[\cos(2\pi f_2 t+\varphi_3)-\cos(2\pi f_2 t_0+\varphi_3)\right] \end{cases} \quad (3)$$

According to Eqs. (1)-(3), single diamond grit particle (G) trajectory can be conveyed as:

$$\begin{cases} x = V_w(t-t_0)+\dfrac{d_s}{2}\sin\left[\omega(t-t_0)\right]+A_1\cos\theta\left[\cos(2\pi f_1 t+\varphi_1)\right. \\ \quad \left.-\cos(2\pi f_1 t_0+\varphi_1)\right]+A_2\sin\theta\left[\cos(2\pi f_1 t+\varphi_2)-\cos(2\pi f_1 t_0+\varphi_2)\right] \\ y = \dfrac{d_s}{2}\cos\left[\omega(t-t_0)\right]-\dfrac{d_s}{2}+A_1\sin\theta\left[\cos(2\pi f_1 t+\varphi_1)\right. \\ \quad \left.-\cos(2\pi f_1 t_0+\varphi_1)\right]+A_2\cos\theta\left[\cos(2\pi f_1 t+\varphi_2)-\cos(2\pi f_1 t_0+\varphi_2)\right] \\ z = A_3\left[\cos(2\pi f_2 t+\varphi_3)-\cos(2\pi f_2 t_0+\varphi_3)\right] \end{cases} \quad (4)$$

It is necessary for two mutually perpendicular simple harmonic oscillations to simultaneously act up to two premises to achieve a stable and closed elliptical trajectory as follows [11]:

(1) The frequency of simple harmonic oscillations in the synthesis must be identical.

(2) The skewing of the two simple harmonic oscillations involving elliptical vibrations is not a multiple of π.

Provided that t_0=0, $\varphi_1=0$, $\varphi_2=\pi/2$, $\varphi_3=0$, the trajectory of a single diamond grit particle in 3D ultrasonic vibration can be written as follows:

$$\begin{cases} x = V_w t+\dfrac{d_s}{2}\sin\left(\dfrac{2v_s}{d_s}t\right)+A_1\cos\theta\cos(2\pi f_1 t-1)+A_2\sin\theta\cos(2\pi f_1 t+\dfrac{\pi}{2}) \\ y = \dfrac{d_s}{2}\cos\left(\dfrac{2v_s}{d_s}t\right)-\dfrac{d_s}{2}+A_1\sin\theta\cos(2\pi f_1 t-1)+A_2\cos\theta\cos(2\pi f_1 t+\dfrac{\pi}{2}) \\ z = A_3\left[\cos(2\pi f_2 t)-1\right] \end{cases} \quad (5)$$

The trajectory of a single abrasive under 2D and 3D ultrasonic vibration-assisted grinding was simulated by the software MATLAB as shown in Fig. 5. It can be seen that the trajectory of a single abrasive particle in 2D ultrasonic vibration-assisted grinding is a sinusoidal curve on the plane, while it is a spiral in space during 3D ultrasonic vibration-assisted grinding. This will be similar to rotary cutting for the existence of a spiral trajectory, and thus it is beneficial to keep the cutting edge sharpened to reduce the grinding temperature.

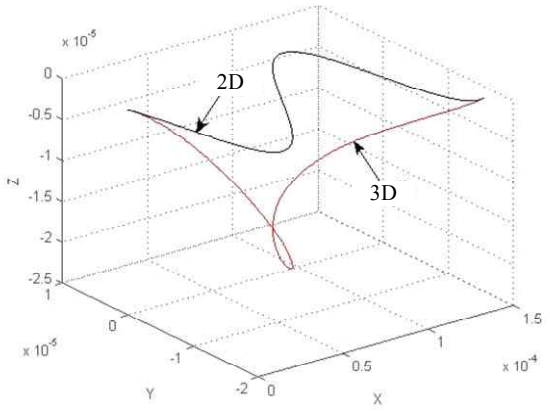

Fig. 5. Simulation results for the trajectory of a single abrasive particle during 2D and 3D ultrasonic vibration grinding.

3.2 The mathematical model of 3D ultrasonic vibration-assisted ELID grinding force

The grinding force is composed mainly of the normal grinding force (F_n) and the tangential grinding force (F_t), while the axial grinding force (F_a) is not frequently considered because it is rather small [12]. By contrast, in 3D ultrasonic vibration-assisted ELID grinding, because high-frequency ultrasonic vibration is introduced in three directions that are mutually perpendicular to each other, the impact approximates into being a greater instantaneous force, which causes the grinding action to increase, namely as normal, tangential and axial impact. Consequently, the grinding force can be expressed as:

$$\begin{cases} F_n = F_{nc} + F_{nf} + F_{nu} \\ F_t = F_{tc} + F_{tf} + F_{tu} \\ F_a = F_{au} \end{cases} \tag{6}$$

where F_{nc} and F_{tc} are the normal force and the tangential force deriving from grinding deformation, respectively, F_{nf} and F_{tf} are the normal force and the tangential force deriving from friction, respectively, and F_{nu}, F_{tu} and F_{au} are the normal force, tangential force and axial force derived from 3D ultrasonic vibration, respectively.

According to Eq. (5), the velocity of a single diamond grit particle during 3D ultrasonic vibrations can be derived as:

$$\begin{cases} V_x = V_w + V_s \cos\left(\dfrac{2V_s t}{d_s}\right) - 2\pi f_1 A_1 \cos\theta \sin 2\pi f_1 t - 2\pi f_1 A_2 \sin\theta \sin(2\pi f_1 t + \dfrac{\pi}{2}) \\ V_y = -V_s \sin\left(\dfrac{2V_s t}{d_s}\right) - 2\pi f_1 A_1 \sin\theta \sin 2\pi f_1 t - 2\pi f_1 A_2 \cos\theta \sin(2\pi f_1 t + \dfrac{\pi}{2}) \\ V_z = -2\pi f_2 A_3 \sin 2\pi f_2 t \end{cases} \tag{7}$$

The cutting arc length from contact to separation in 3D ultrasonic vibrations can be written as:

$$l_g = \int_{t_0}^{t} \sqrt{V_x^2 + V_y^2 + V_z^2}\, d_t \,, \tag{8}$$

where V_x, V_y, and V_z are the diamond grit speed in three coordinate direction, respectively.

In the period $t_0 \sim t$, the volume of materials being removed can be expressed as:

$$V_c = a_p b V_w \,, \tag{9}$$

where a_p is the actual grinding depth, and b is the grinding width.

In the time of $t_0 \sim t$, the number of effective grit particles taking part in grinding is given as the following equation [8]:

$$N_l = N_v V_a = \frac{6V_m}{\pi d^3} \frac{bl}{d_s} (d_s - h - d)(d - h) \tag{10}$$

where N_l denotes effective number grit particle's in the arc segment, N_v is the number of unit volumes, V_a is the effective volume in the arc segment, V_m is the volume fraction of the grinding grit, h is the thickness of the oxide film, l is the contact arc length, and d is the grit diameter.

During the process of electrolytic in-process dressing metal-bonded diamond grinding wheel, the equation can be expressed as follows, according to Faraday's law of electrolysis:

$$\frac{dV_v}{dt} = \eta \frac{MI}{zF\rho} \,, \tag{11}$$

where V_v is the volume of removal bonded metal, t is the effective electrolytic time, η is the current efficiency, M denotes the molecular weight of the bonded metal, z is the valency of the metal, ρ is the density of the bonded metal, and F is the Faraday constant.

The removed bonded-metal volume can be defined as:

$$V_v = \eta \frac{MIt_e}{zF\rho} \,. \tag{12}$$

The average electrolytic thickness on anode be expressed as:

$$l_e = \eta \frac{MIt_e}{zF\rho A_a} \,, \tag{13}$$

where A_a is the effective conductive area of the anode.

Ohm's law is shown as:

$$I = \frac{U}{R} \,. \tag{14}$$

In ELID grinding, the total resistance R includes the electrolyte resistance R_e and the oxidation film resistance R_0, as is shown Eq. (15):

$$R = R_e + R_0 = \frac{\rho_e h_e}{A_e} + \frac{\rho_0 h}{A_e}, \tag{15}$$

where ρ_e is the resistivity for ELID electrolyte, h_e is the inter-electrode clearance, ρ_0 is the resistivity of the oxide film, and A_e is the effective area of the cathode.

Substituting Eq. (15) into Eq. (14), the current *I* can be obtained as.

$$I = \frac{U}{R} = \frac{UA_e}{\rho_e h_e + \rho_o h}. \tag{16}$$

According to Eqs. (13) and (16), the thickness of the dissolved anode layer can be derived as:

$$l_e = \eta \frac{MIt_e}{zF\rho A_a} = \frac{\eta M t_e U A_e}{zF\rho A_a(\rho_e h_e + \rho_o h)}. \tag{17}$$

During the ELID grinding, the actual grinding depth can be expressed as:

$$a_p = a_p' - l_e = a_p' - \frac{\eta M t_e U A_e}{zF\rho A_a(\rho_e h_e + \rho_o h)}, \tag{18}$$

where $a_p^{'}$ is the nominal grinding depth.

The volume of material removed by a single diamond grit particle can be derived as:

$$V_g = \frac{V_c}{N} = \frac{a_p V_w}{RV_s}. \tag{19}$$

The average area of cutting section (S_g) of a single diamond grit particle can be expressed as:

$$S_g = \frac{V_g}{l_g} = \frac{a_p V_w}{RV_s \int_{t_0}^{t} \sqrt{V_x^2 + V_y^2 + V_z^2}\, d_t} \tag{20}$$

Based on the average cutting section area, the normal grinding force F_{gnc} of a single diamond grit particle is proportional to the cross-sectional area of the cut, and the equation can be expressed as [13]:

$$F_{\mathrm{gnc}} = KS_{\mathrm{g}}, \tag{21}$$

where *K* is a constant.

Taking into consideration the normal force acting in front of the diamond grit particle, and assuming that the frictional force between the chip and the grit can be neglected, it can be assumed that the grinding particle is conical and the following equation can be obtained according to geometric relationships:

$$\frac{F_{\mathrm{gnc}}}{F_{\mathrm{gtc}}} = \frac{4}{\pi}\tan\theta. \tag{22}$$

Combining Eqs. (20)-(22), the normal force F_{gnc} and the tangential force F_{gtc} of single diamond grit particle can be written as:

$$\begin{cases} F_{gnc} = \dfrac{Ka_p V_w}{RV_s \int_{t_0}^{t} \sqrt{V_x^2 + V_y^2 + V_z^2}\, d_t} \\ F_{gtc} = \dfrac{\pi K a_p V_w}{4(\tan\theta) RV_s \int_{t_0}^{t} \sqrt{V_x^2 + V_y^2 + V_z^2}\, d_t} \end{cases} \tag{23}$$

In the period $t_0 \sim t$, the normal force F_{nc} and the tangential force F_{tc} deriving from grinding deformation can be expressed as:

$$\begin{cases} F_{nc} = N_l F_{gnc} = RblF_{gnc} = \dfrac{Kbl[zF\rho A_a(\rho_e h_e + \rho_o h)a_p' - \eta M t_e U A_e]V_w}{V_S zF\rho A_a(\rho_e h_e + \rho_o h)\int_{t_0}^{t} \sqrt{V_x^2 + V_y^2 + V_z^2}\, d_t} \\ F_{tc} = N_l F_{\mathrm{gtc}} = \dfrac{\pi Rbl}{4\tan\theta} F_{\mathrm{gtc}} = \dfrac{\pi Kbl[zF\rho A_a(\rho_e h_e + \rho_o h)a_p' - \eta M t_e U A_e]V_w}{4(\tan\theta)V_S zF\rho A_a(\rho_e h_e + \rho_o h)\int_{t_0}^{t} \sqrt{V_x^2 + V_y^2 + V_z^2}\, d_t} \end{cases} \tag{24}$$

In 3D ultrasonic vibration-assisted ELID grinding, the normal force F_{gnf} and the tangential force F_{gtf} deriving from friction can be expressed as:

$$\begin{cases} F_{gnf} = \delta p \\ F_{gtf} = \mu \delta p \end{cases} \tag{25}$$

where δ is the surface area of a single diamond grit particle, which is equivalent to the actual contact area between workpiece and the grit; p denotes the even contact pressure between the wear surface and the workpiece, and μ is the sliding friction coefficient.

In the period of $t_0 \sim t$, the normal force F_{gnf} and the tangential force F_{gtf} deriving from friction can be expressed as:

$$\begin{cases} F_{nf} = N_l F_{gnf} = \dfrac{6V_m}{\pi d^3}\dfrac{bl}{d_s}(d_s - h - d)(d - h)\delta P \\ F_{tf} = N_l F_{gtf} = \mu \dfrac{6V_m}{\pi d^3}\dfrac{bl}{d_s}(d_s - h - d)(d - h)\delta P \end{cases} \tag{26}$$

Provided $t_0 = 0$, $\varphi_1 = 0$, $\varphi_2 = \pi/2$, $\varphi_3 = 0$, according to Eq. (5), the velocity and acceleration of the particle at t moment caused by 3D ultrasonic vibration can be conveyed as:

$$\begin{cases} V_x = -2\pi f_1 A_1 \cos\theta \sin 2\pi f_1 t - 2\pi f_1 A_2 \sin\theta \sin(2\pi f_1 t + \dfrac{\pi}{2}) \\ V_y = -2\pi f_1 A_1 \sin\theta \sin 2\pi f_1 t - 2\pi f_1 A_2 \cos\theta \sin(2\pi f_1 t + \dfrac{\pi}{2}) \\ V_z = -2\pi f_2 A_3 \sin 2\pi f_2 t \end{cases} \tag{27}$$

$$\begin{cases} a_x = A_1(2\pi f_1)^2 \cos\theta\cos 2\pi f_1 t - A_2(2\pi f_1)^2 \sin\theta\cos(2\pi f_1 t + \dfrac{\pi}{2}) \\ a_y = A_1(2\pi f_1)^2 \sin\theta\cos 2\pi f_1 t - A_2(2\pi f_1)^2 \cos\theta\cos(2\pi f_1 t + \dfrac{\pi}{2}) \\ a_z = -A_3(2\pi f_2)^2 \cos 2\pi f_2 t \end{cases} \tag{28}$$

Based on momentum theory, the average impact of the particles in the grinding wheel in three directions can be approximately defined as:

$$\begin{cases} F_{tu} = \dfrac{Mv_{x2} - Mv_{x1}}{\Delta t} = \dfrac{2\pi Mf_1}{\Delta t}\left\{\begin{matrix}[-A_1\cos\theta\sin 2\pi f_1(t+\Delta t) - A_2\sin\theta\sin[2\pi f_1(t+\Delta t)+ \\ \dfrac{\pi}{2}] + A_1\cos\theta\sin 2\pi f_1 t + A_2\sin\theta\sin(2\pi f_1 t + \dfrac{\pi}{2})\end{matrix}\right\} \\ \quad \approx -(2\pi f_1)^2 M[A_1\cos\theta\cos 2\pi f_1 t + A_2\sin\theta\cos(2\pi f_1 t + \dfrac{\pi}{2})] \\ F_{nu} = \dfrac{Mv_{y2} - Mv_{y1}}{\Delta t} = \dfrac{2\pi Mf_1}{\Delta t}\left\{\begin{matrix}[-A_1\sin\theta\sin 2\pi f_1(t+\Delta t) - A_2\cos\theta\sin[2\pi f_1(t+\Delta t)+ \\ \dfrac{\pi}{2}] + A_1\sin\theta\sin 2\pi f_1 t + A_2\cos\theta\sin(2\pi f_1 t + \dfrac{\pi}{2})\end{matrix}\right\} \\ \quad \approx -(2\pi f_1)^2 M[A_1\sin\theta\cos 2\pi f_1 t + A_2\cos\theta\cos(2\pi f_1 t + \dfrac{\pi}{2})] \\ F_{au} = \dfrac{Mv_{z2} - Mv_{z1}}{\Delta t} = \dfrac{2\pi Mf_2 A_3}{\Delta t}[-\sin 2\pi f_2(t+\Delta t) + \sin 2\pi f_2 t] \\ \quad \approx -(2\pi f_2)^2 MA_3\cos 2\pi f_2 t \end{cases} \tag{29}$$

where M is the equivalent mass of the vibrating part.

According to Eqs. (24), (26) and (29), the grinding force including the tangential force (F_t), the normal force (F_n) and the axial force (F_a) in 3D ultrasonic vibration-assisted ELID internal grinding can be expressed as:

$$\begin{cases} F_t = \dfrac{\pi Kbl[zF\rho A_a(\rho_e h_e + \rho_o h)a'_p - \eta Mt_e UA_e]V_w}{4(\tan\theta)V_s zF\rho A_a(\rho_e h_e + \rho_o h)\int_{t_0}^{t}\sqrt{V_x^2 + V_y^2 + V_z^2}\,dt} + \mu\dfrac{6V_m}{\pi d^3}\dfrac{bl}{d_s}(d_s - h - d)(d - h)\delta P \\ \quad -(2\pi f_1)^2 M[A_1\cos\theta\cos(2\pi f_1 t) + A_2\sin\theta\cos(2\pi f_1 t + \dfrac{\pi}{2})] \\ F_n = \dfrac{Kbl[zF\rho A_a(\rho_e h_e + \rho_o h)a'_p - \eta Mt_e UA_e]V_w}{V_s zF\rho A_a(\rho_e h_e + \rho_o h)\int_{t_0}^{t}\sqrt{V_x^2 + V_y^2 + V_z^2}\,dt} + \dfrac{6V_m}{\pi d^3}\dfrac{bl}{d_s}(d_s - h - d)(d - h)\delta P \\ \quad -(2\pi f_1)^2 M[A_1\sin\theta\cos(2\pi f_1 t) + A_2\cos\theta\cos(2\pi f_1 t + \dfrac{\pi}{2})] \\ F_a = -(2\pi f_2)^2 MA_3\cos(2\pi f_2 t) \end{cases} \tag{30}$$

From what has been discussed above, as shown Eq. (30), the conclusion can be drawn that the grinding forces, F_t and F_n, in 3D ultrasonic vibration-assisted ELID grinding, increase along with the grinding width (b), the contact arc length (l), the actual grinding depth (a_p) and the speed of workpiece (V_w). By contrast, the forces decrease with increasing speed of the grinding wheel (V_s), and the frequency of 2D the ultrasonic vibration (f_1), and the ultrasonic amplitude A_1 and A_2 increase. In addition, the grinding force F_a increases with axial ultrasonic frequency f_2 and amplitude A_3 .

4. Experimental tests and analyses of grinding force

4.1 Testing setup and methodology

The 3D ultrasonic vibration-assisted ELID grinding tests involved using a modified CNC machining center (VMC850E) assisted by a purpose-designed ultrasonic vibration device. The apparatus was mainly composed of an ultrasonic vibration system, dynamic dynamometer, and spark-erosion machining device, as shown in Fig. 6. The ultrasonic vibration system comprised the ultrasonic generator, electric transmission device, ultrasonic wave transducer, amplitude transformer, and grinding wheel. The grinding force during processing was recorded by an ultra-precision grinding force measurement system (SDC-CJ3SA). The material of the workpiece was zirconia ceramic.

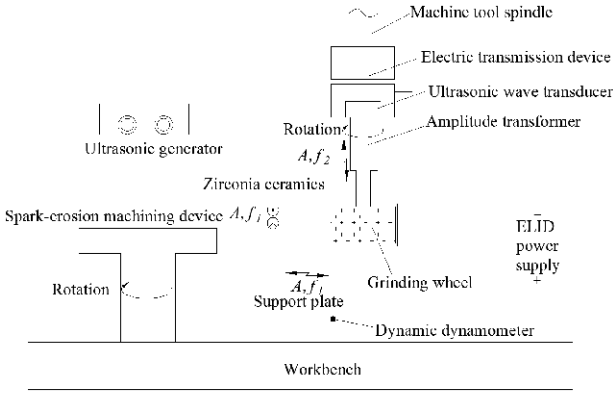

Fig. 6. Platform schematic of the 3D ultrasonic vibration-assisted ELID internal grinding set-up.

It was necessary for the grinding wheel to be dressed by spark-erosion machining before grinding, which then undertook the ultrasonic vibration-assisted ELID grinding. During grinding, the rotation speed of the grinding wheel (n_s) and the workpiece (V_w), the actual grinding depth (a_p) and duty ratio (D) were the primary factors influencing the grinding force. Single-factor tests were conducted and the basic parameters of the rotation speed of the grinding wheel (n_s = 3000 r/min), the speed of the workpiece (V_w = 80 mm/min) and the actual grinding depth (a_p = 0.003 mm) were adapted, and only one of the basic parameters was changed during each group test in order to evaluate the variation in the 3D ultrasonic vibration-assisted ELID grinding force for each different factor. During the tests, 2D and 3D ultrasonic vibration-assisted ELID grinding was achieved by switching on or off the power supply to the ultrasonic transducer in the spindle of the machining center. Three repeated tests were carried out on each set of parameters under these two processing methods and the average value of the parameter under examination was taken as the result of the set of tests to minimize errors. The materials, relevant data collection devices and machine tool models used in the experiment are shown in Table 1.

To achieve the elliptical vibration trajectory, $\varphi_1 = 0$, $\varphi_2 = \pi/2$ was selected in the tests, and two ultrasonic generators (35 kHz) provided simultaneous input for the 2D ultrasonic vibration system. The test equipment is shown in Fig. 7.

The grinding force waveform diagram for 2D and 3D ultrasonic vibration-assisted ELID internal grinding is shown in Figs.

Table 1. Grinding force testing device.

Category	Type	Parameter
Metal-bonded diamond grinding wheel	Bonded Size (mm) Diameter (mm) Height (mm) Abrasive thickness (mm)	Cast iron fiber 1.250~1.6 25 17 3.5
Grinding fluid made in HIT	Dilution ratio	1:50
High frequency pulse power of ELID mirror grinding	HDMD-V	-
Zirconia ceramics specimen	L×W×H(mm)	16 ×16 ×8
Ultrasonic generator	SZ12	-
Impedance analyzer	PV70A	-
Ultra-precision grinding force measurement system	SDC-CJ3SA Measurement range Accuracy	 0~250 N 0.02 N

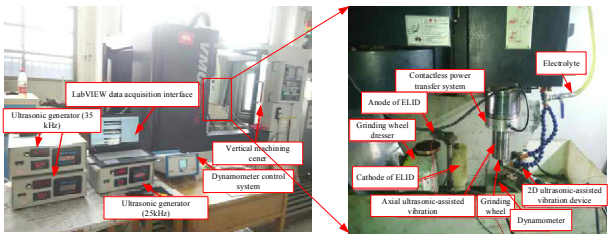

Fig. 7. 3D ultrasonic vibration-assisted ELID internal grinding test equipment.

8(a) and (b), respectively. It can be seen that the shape of the grinding force waveform diagram retains coherence in the two situations. However, the peak of grinding force was relatively smaller during the latter 3D condition. Additionally, because the grinding force (F_Z) along Z direction was relatively lower than in the other direction, F_Z could be neglected during the tests. Furthermore, from Fig. 8, the grinding force in 3D ultrasonic vibration-assisted ELID internal grinding decreased by 20 %-30 % compared to that during 2D ultra-sonic vibration-assisted ELID internal grinding.

4.2 Analysis of the grinding force

4.2.1 Influence of process parameters on the grinding force

As described in Sec. 3.2, the grinding force could be predicted using the mathematical model for 3D ultrasonic vibration-assisted ELID grinding force. The predicted force was obtained when the process parameters were selected as the rotation speed of the grinding wheel (n_s), the speed of the workpiece (V_w), and the grinding depth (a_p). The variation of grinding force with speed of grinding wheel (n_s) is shown in Fig. 9. As is evident from Fig. 9, the grinding force under 3D ultrasonic vibration-assisted ELID grinding was lower than that

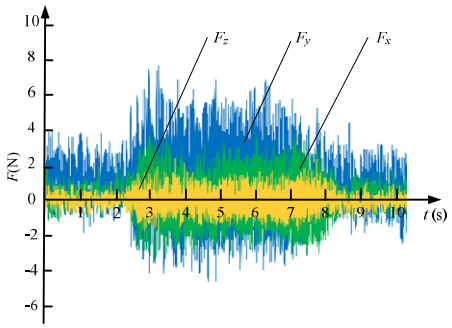

(a) 2D ultrasonic vibration-assisted ELID internal grinding

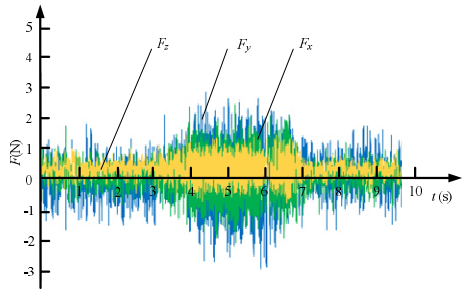

(b) 3D ultrasonic vibration-assisted ELID internal grinding

Fig. 8. Grinding force waveform diagram for 2D and 3D ultrasonic vibration-assisted ELID grinding.

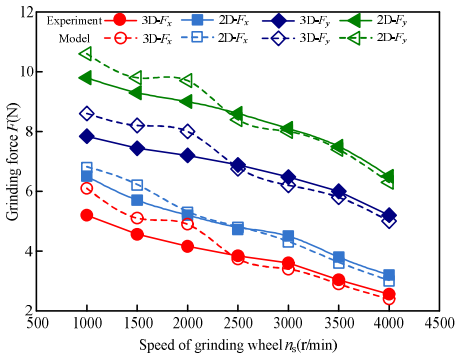

Fig. 9. Relationship between the grinding force and the speed of the grinding wheel.

under 2D ultrasonic vibration-assisted ELID grinding. In addition, the grinding force decreased with any increase in the speed of the grinding wheel. This was attributed to the fact that the effective number of grit particles that take part in grinding increases as the speed of the grinding wheel increases. However, the total grinding resistance is unvaried, and the average contact area between diamond grit particles and workpiece in unit time increases more and more dramatically, which brings about a decrease in the grinding force per unit area. In particular, the grinding force decreases significantly if the speed of the grinding wheel is more than 3000 r/min.

The relationship between the grinding force and the speed of workpiece is presented in Fig. 10. As shown, the grinding force increases with an increase in the speed of workpiece. The

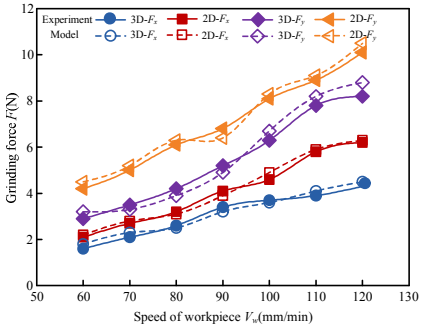

Fig. 10. Relationship between the grinding force and the speed of the workpiece.

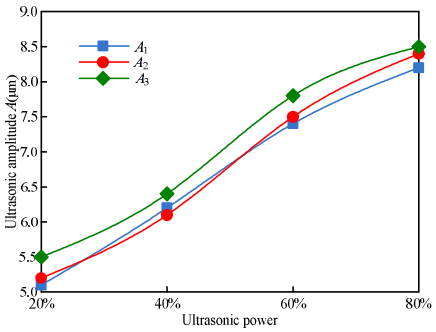

Fig. 12. Relationship between the ultrasonic power and ultrasonic amplitude.

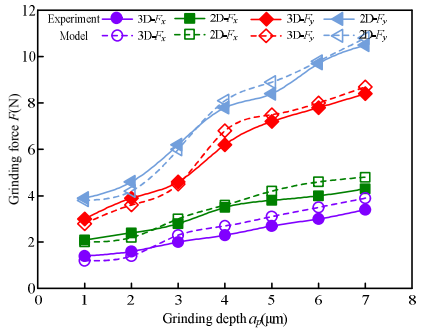

Fig. 11. Relationship between the grinding force and the grinding depth.

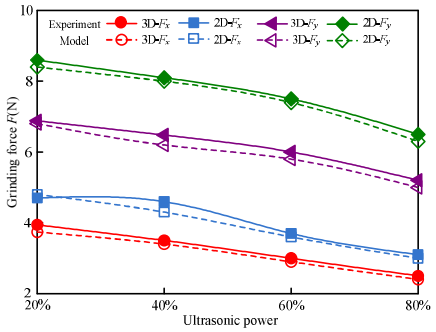

Fig. 13. Relationship between grinding force and ultrasonic power.

grinding force under 3D ultrasonic vibration-assisted ELID grinding was lower than was that under 2D. This was because the grinding method during the tests was down-grinding, and the grinding wheel speed was greater than the workpiece speed. An increase in the speed of the workpiece makes the relative speed between the grinding wheel and the workpiece decrease, and the average contact time between the grinding grains and the workpiece being processed in unit time is shorter. In the case that the total grinding force is unchanged, the grinding force per unit area decreases.

The relationship between the grinding force and grinding depth is shown in Fig. 11. The grinding force was observed to increase when the grinding depth ranged from 1 μm to 7 μm. This is due mainly to the following reasons: With an increase in the grinding depth, the actual cutting thickness for grinding grains located on the outer layer of grinding wheel increases, and the undeformed cutting thickness for a single grinding grain particle increases, so the resistance generated by the grinding grain cutting into the workpiece material increases and the grinding force also increases. In addition, with the increase in grinding depth, the extrusion force between the oxide film on the outer layer of the grinding wheel and the workpiece increases, and the heat generated during grinding, and extrusion force in the grinding process, will cause the relatively loose soft oxide film to be compacted, so the grinding force also will increase.

In addition, from Fig. 11, when the grinding depth was greater than 3 μm, the grinding force suddenly increased significantly. The main reason may be that the grinding depth exceeds the critical grinding depth of plastic domain processing for zirconia ceramic, changing the status of the method of material removal from plastic removal into brittle removal, and in consequence, the grinding force is increased. Besides, the application of axial ultrasonic vibration to the workpiece material causes vibration stress inside the material, offsetting some of the original stress within the material, thereby reducing the hardness of the material. In consequence, it is easier for the grinding grains on outer layers of the grinding wheel to cut the workpiece material so that, under three-dimensional grinding, the grinding force is smaller.

4.2.2 Influence of ultrasonic parameters on the grinding force

It is well known that the ultrasonic amplitude exhibits a significant effect on the grinding force [14]. During the tests, because it was difficult to control directly the ultrasonic amplitude, according to Wang et al. [15], the ultrasonic power could be utilized to effect variations in the amplitude of the ultrasonic impulses. The relationship between ultrasonic power and amplitude is shown in Fig. 12. The effect of ultrasonic amplitude on the grinding force could be inferred from tuning the power supplied to the ultrasonic generator. The effect of the power of the ultrasonic impulse on the grinding force is presented in Fig. 13.

It can be observed from Fig. 13 that the grinding force decreased with an increase in ultrasonic power. This may be due

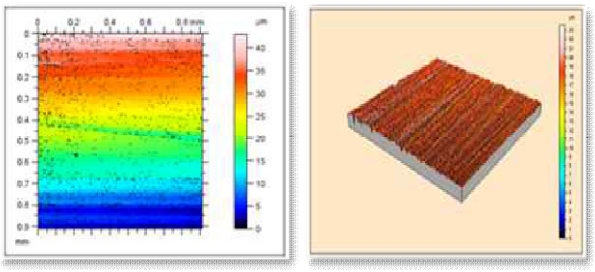

(a) Surface profile after 2D ultrasonic vibration-assisted ELID grinding

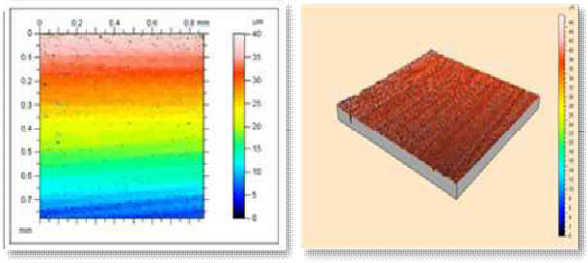

(b) Surface profile after 3D ultrasonic vibration-assisted ELID grinding

Fig. 14. Surface roughness from 2D and 3D ultrasonic vibration-assisted ELID internal grinding.

to an increase in the amplitude of the ultrasonic signal resulting in an increase in the contact length of the grinding wheel to the workpiece per unit of time, and therefore also an increase in the average contact area. If the total grinding force is unchanged, the average grinding force in a unit area is reduced. In addition, it was concluded that the normal force and the tangential force under 3D ultrasonic vibration-assisted ELID grinding was lower than was that during 2D grinding. It was observed that the results of the physical tests were consistent with the calculated predictions. The 3D ultrasonic vibration system was designed especially for the experiment, and therefore the frequency of the vibration system could not be changed over a wide range. However, a slight change in ultrasonic frequency would not influence dramatically the ultrasonic amplitude. If the frequency deviated from the resonant frequency, the ultrasonic vibration would be suppressed or might even stop vibration. Thus, the effect of frequency on the grinding force was not considered during the present tests, but future studies will consider this issue.

4.3 Surface quality in 3D ultrasonic vibration-assisted internal grinding

To observe effectively the surface quality of the machined workpiece, the specimen had to be clean and dry. Taking three points on the finished surface, measurements of the roughness of the surface were made and a final average value was obtained by averaging the measured results. The surface roughness was tested using a contactless Talysurf CCI6000 and a 3D white-light interference surface profilometer made in Taylor Hobson Co., Ltd. In 3D ultrasonic vibration-assisted ELID internal grinding, surface irregularity was relatively small, and the

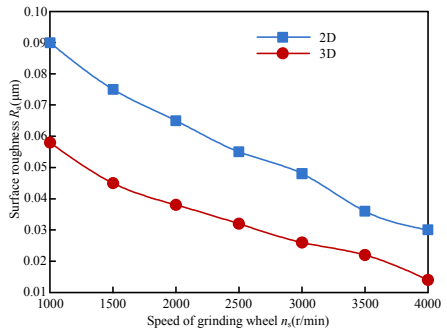

(a) Speed of the grinding wheel

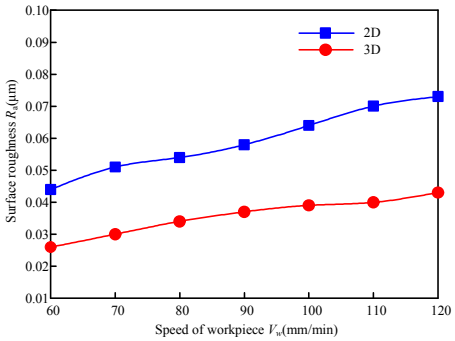

(b) Speed of the workbench

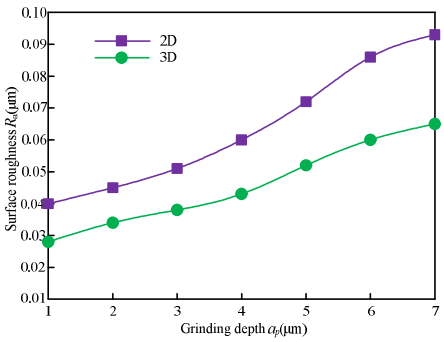

(c) Grinding depth

Fig. 15. Surface roughness for 2D and 3D ultrasonic vibration-assisted ELID internal grinding for different process parameters.

surface profile was relatively flat. The Ra was 0.01378 μm for 3D ultrasonic vibration-assisted internal grinding was less than that of 0.06157 μm for 2D ultrasonic vibration-assisted ELID grinding, as is shown in Fig. 14.

4.3.1 Influence of process parameters on the surface roughness

The variation in roughness with changes in process parameters was analyzed from the test results, as shown in Fig. 15. Overall, the roughness (Ra) values for 3D grinding fell by 40 % to 50 % compared with 2D ultrasonic vibration-assisted ELID internal grinding and retained better surface quality. From Fig. 15(a), the conclusion can be drawn that with the increase in speed of the grinding wheel from 1000 to 4000 r/min, that more diamond grit particles take part in cutting for a longer period,

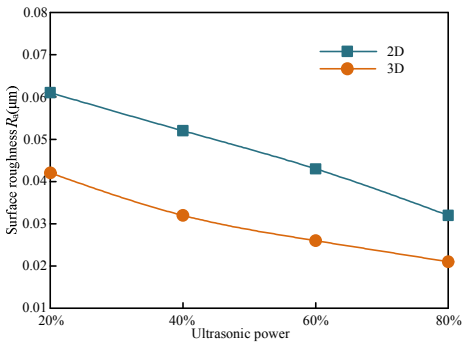

Fig. 16. Variation in surface roughness for 2D and 3D ultrasonic vibration-assisted ELID grinding under different ultrasonic power.

and increase the number of its score in machining surface, which prolongs the cutting trajectory, reduces the surface roughness and enhances the surface quality. From Fig. 15(b), because the cutting arc length for a single diamond grit particle effectively increases, the period of exposure to the sharp edges of the grit is prolonged and, ignoring the effect of any grinding fluid, when the speed of workbench was gradually increased from 60 to 120 mm/min, the roughness (Ra) for 3D ultrasonic vibration-assisted ELID internal grinding was lower and a better surface quality was obtained than was the case for 2D ultrasonic vibration-assisted ELID internal grinding.

From Fig. 15(c), with the grinding depth gradually increased from 0.001 to 0.007mm during the process, and whether it was two-dimensional ultrasonic ELID composite inner round grinding or three-dimensional ultrasonic ELID composite inner cylindrical grinding, the workpiece surface roughness gradually increased, and the change was very obvious. In addition, it can be observed that the surface roughness of the workpiece after three-dimensional ultrasonic ELID composite internal grinding was lower than that after two-dimensional ultrasonic ELID composite internal grinding of the workpiece. This verification of the effectiveness of 3D ultrasonic auxiliary grinding obtained from analysis of Eq. (5) demonstrated that the length of the cutting arc of a single grinding particle is effectively increased during the cutting process, and will maintain its sharp cutting edge for a long time, and is enhanced by timely reduction of the grinding temperature on the surface of the workpiece. This shows that lower surface roughness is produced by three-dimensional ultrasonic ELID composite internal cylindrical grinding than can be obtained from 2D ultrasonic ELID composite internal cylindrical grinding.

4.3.2 Influence of ultrasonic parameters on the surface roughness

The variation in surface roughness from 2D and 3D ultrasonic vibration-assisted ELID grinding under different ultrasonic power is shown in Fig. 16. The surface roughness in both cases decreased with an increase in ultrasonic power. The surface roughness in 3D ultrasonic vibration-assisted ELID grinding was lower than that for 2D ultrasonic vibration-assisted ELID grinding. This was attributed to the fact that the ultrasonic amplitude increased with the increase in the ultrasonic power, which produced cutting grooves that were wider than those in 2D ultrasonic vibration-assisted ELID grinding. In addition, the action of axial ultrasonic vibration on the grinding wheel enhanced the length of the trajectory of the abrasive. Therefore, the surface roughness decreased in the 3D ultrasonic vibration-assisted ELID grinding.

5. Conclusions

(1) The grinding force was established during 3D ultrasonic vibration-assisted ELID internal grinding and was analyzed in terms of its effect on a composite grinding system utilizing ultrasonic vibration-assisted ELID for internal grinding of a cylindrical bore and the kinematics analysis of the trajectory of a single diamond grit particle. The theoretical analysis and mathematical model were verified to be reliable and valid.

(2) During 3D ultrasonic vibration-assisted ELID internal grinding, the grinding force was decreased by 20 %-30 % compared to that for 2D ultrasonic vibration-assisted ELID internal grinding, which confirmed the superior capability of the 3D ultrasonic-vibration assisted ELID approach.

(3) The cutting arc length of a single diamond grit particle effectively was increased and the retention period of sharp edges on the grit particles was prolonged during 3D ultrasonic vibration-assisted ELID internal grinding, which led to an improvement in surface quality a decrease in surface roughness (Ra) by 40 % to 50 % compared with 2D ultrasonic vibration-assisted ELID internal grinding.

Conflict of Interest

The authors declare that there is no conflict of interest regarding the publication of this paper.

Acknowledgments

The authors sincerely acknowledge the National Science Foundation of China (Grant No. 51805284) and the key scientific research projects in colleges and universities in Henan Province (Grant No. 19A460006). This project is supported by the Henan Zhongyuan Ancient Ceramic Key Laboratory. Sincere thanks to the reviewers for their professional suggestions on this study.

Nomenclature

f_1 : Frequency of 2D ultrasonic vibration on workbench with the synchronous vibration
f_2 : Frequency in Z direction
θ : Fixed angle of L plate
A_1 : Ultrasonic amplitude in X direction
A_2 : Ultrasonic amplitude in Y direction
A_3 : Ultrasonic amplitude in Z direction
φ_1 : Ultrasonic vibration phase angle

φ_2 : Ultrasonic vibration phase angle
φ_3 : Ultrasonic vibration phase angle
V_s : Speed of grinding wheel
V_w : Speed of workpiece
n_s : Rotation speed of grinding wheel
ω : Angular speed of grinding wheel
d_s : Diameter of grinding wheel
Fn : Normal grinding force
Ft : Tangential grinding force
Fa : Axial grinding force grinding force
F_{gnc} : Diamond grit normal force deriving from grinding deformation
F_{nc} : Normal force deriving from grinding deformation
F_{gtc} : Diamond grit tangential force deriving from grinding deformation
F_{tc} : Tangential force deriving from grinding deformation
F_{gnf} : Diamond grit normal force deriving from friction
F_{nf} : Normal force deriving from friction
F_{gtf} : Diamond grit tangential force deriving from friction
F_{tf} : Tangential force deriving from friction
F_{nu} : Normal force deriving from3D ultrasonic vibrations
F_{tu} : Tangential force deriving from3D ultrasonic vibrations
F_{au} : Axial force deriving from 3D ultrasonic vibrations
V_x : The diamond grit speed in X direction
V_y : The diamond grit speed in Y direction
V_z : The diamond grit speed in Z direction
a_p : Actual grinding depth
a_p' : Nominal grinding depth
b : Grinding width
N_l : Effective grits' number in arc segment
N_v : The number of unit volume,
V_a : Effective volume in arc segment
V_m : The volume fraction of grinding grit
δ : The surface area of single diamond grit
p : Evenly contact pressure between wear surface and workpiece
μ : Sliding friction coefficient
h : Thickness of oxide film
l : Contact arc length
d : Grit diameter
V_v : Volume of removal metal-bonded
η : Current efficiency
M : Molecular weight of metal-bonded
z : Valence of metal
ρ : Density of metal-bonded
F : Faraday constant.
A_a : Effective area of anode for conduction
R : Total resistance
R_e : Electrolyte resistance
R_0 : Oxidation film resistance
ρ_e : Electrolyte resistivity
h_e : Inter-electrode clearance
ρ_o : Oxidation film resistivity
A_e : Effective area of cathode
U : Electrode voltage

References

[1] K. Wongkamhaeng, D. V. Dawson and J. A. Holloway, Effect of surface modification on in depth transformations and flexural strength of zirconia ceramics, *J. of Prosthodontics*, 28 (1) (2019) 364-375.

[2] A. Yurdakul and H. Gocmez, One-step hydrothermal synthesis of yttria-stabilized tetragonal zirconia polycrystalline nanopowders for blue-colored zirconia-cobalt aluminate spinel composite ceramics, *Ceramics International*, 45 (5) (2019) 5398-5406.

[3] B. M. A. Abdo, N. Ahmed and M. E. Abdulaziz, Laser beam machining of zirconia ceramic: An investigation of micromachining geometry and surface roughness, *J. of Mechanical Science and Technology*, 33 (4) (2019) 1817-1831.

[4] Y. Q. Wen, J. Y. Tang and W. Zhou, Study on contact performance of ultrasonic-assisted grinding surface, *Ultrasonics*, 91 (2019) 193-200.

[5] Y. Wang, Y. Dong and H. Guang, Study on key factors influencing the surface generation in rotary ultrasonic grinding for hard and brittle materials, *J. of Manufacturing Processes*, 38 (2019) 549-555.

[6] Z. Q. Liang, Y. B. Wu and X. B. Wang, A new two-dimensional ultrasonic assisted grinding (2D-UAG) method and its fundamental performance in monocrystal silicon machining, *International J. of Machine Tools and Manufacture*, 50 (5) (2010) 728-736.

[7] Y. Y. Yan, B. Zhao and J. L. Liu, Ultraprecision surface finishing of nano-ZrO_2 ceramics using two-dimensional ultrasonic assisted grinding, *International J. of Advanced Manufacturing Technology*, 43 (5-6) (2009) 462-467.

[8] B. Zhao, Z. Liu and Y. Zheng, Grinding force modeling for ultrasonic ELID composite grinding, *Aerospace Material & Technology*, 4 (2014) 31-35.

[9] G. Q. Yin, Y. D. Gong and Y. W. Li , Research on force and temperature characteristics of novel point grinding wheels. *J. of Mechanical Science and Technology*, 32 (8) (2018) 3817-3834.

[10] Z. Bo, C. Fan and X. F. Jia, Surface quality prediction model of nano-composite ceramics in ultrasonic vibration-assisted ELID mirror grinding, *J. of Mechanical Science and Technology*, 31 (4) (2017) 1877-1884.

[11] Y. Y. Yan, *Study on Two Dimensional Ultrasonic Vibration Assisted Grinding Mechanism of Nanocomposite Ceramic and Its Surface Quality*, Shanghai Jiao Tong University, Shanghai, China (2008).

[12] Y. Gong, Y. Zhou and X. Wen, Experimental study on micro-grinding force and subsurface microstructure of nickel-based single crystal superalloy in micro grinding, *J. of Mechanical Science and Technology*, 31 (7) (2017) 3397-3410.

[13] X. Z. Xiao, K. Zheng and W. H. Liao, Study on cutting force model in ultrasonic vibration assisted side grinding of zirconia ceramics, *International J. of Machine Tools & Manufacture*, 104 (2016) 58-67.

[14] F. C. Hai, Y. T. Jin and S. Wen, An investigation of surface

roughness in ultrasonic assisted dry grinding of $12Cr_2Ni_4A$ with large diameter grinding wheel, *International J. of Precision Engineering and Manufacturing*, 19 (6) (2018) 929-936.
[15] J. Wang, P. Feng and J. Zhang, Experimental investigation on the effects of thermomechanical load on the vibrational stability during rotary ultrasonic machining, *Machining Science and Technology*, 21 (2) (2016) 239-256.

Fan Chen received her Ph.D. in School of Mechanical and Power Engineering from Henan Polytechnic University of Jiaozuo, China, in 2017. Now she works at School of Electrical and Mechanical Engineering, Pingdingshan University, Pingdingshan, 467000, China. Her current research interests are in precision, super precision manufacturing technology, especially in the technology of ultrasonic vibration-assisted machining.